Photoelectrochemical activation of peroxymonosulfate using Sn-doped α-Fe₂O₃ thin film for degradation of anti-inflammatory pharmaceutical drug

Manel Machreki [a], Georgi Tyuliev [b], Dušan Žigon [c], Qian Guo [d], Takwa Chouki [a], Ana Belén Jorge Sobrido [d], Stoichko Dimitrov [e], Saim Emin [a,*]

[a] Materials Research Laboratory, University of Nova Gorica, Vipavska 11c, 5270 Ajdovščina, Slovenia
[b] Institute of Catalysis, Bulgarian Academy of Sciences, Acad. G. Bonchev St, Bldg. 11, Sofia 1113, Bulgaria
[c] Institute "Jožef Stefan", Jamova 39, 1000 Ljubljana, Slovenia
[d] School of Engineering and Material Science, Queen Mary University of London, E1 4NS London, U.K
[e] School of Physical and Chemical Sciences, Queen Mary University of London, E1 4NS London, U.K

ARTICLE INFO

ABSTRACT

Introduction of oxygen vacancies (OVs) has been investigated as a promising way to improve the electrical and catalytic characteristics of a hematite (α-Fe₂O₃) based photoelectrode. In this work, we develop a novel method for preparing porous Sn-doped α-Fe₂O₃ (Sn:Fe₂O₃) thin films with intrinsic OVs. The procedure included spin-coating an iron precursor onto a fluorine-doped tin oxide (FTO) substrate, followed by thermal treatment at elevated temperatures. The influence of Sn dopant on the optoelectronic properties of α-Fe₂O₃ was demonstrated by X-ray photoelectron spectroscopy and photoelectrochemical (PEC) measurements. The combined effect of OVs and Sn doping was found to play a synergistic role in reducing the charge recombination's. The Sn:Fe₂O₃ photoanodes were used as a dual catalyst to oxidise water and break down an anti-inflammatory drug called 2-(4-isobutylphenyl)propanoic acid (IBPA). The Sn:Fe₂O₃ thin film with a 30-minute heat treatment time displayed the highest incident photon-to-current efficiency. For the first time, Sn:Fe₂O₃ thin films were utilised in the effective PEC degradation of IBPA employing peroxymonosulfate (PMS) under visible light illumination. The hydroxyl radicals (•OH), singlet oxygen ($^1O_2$), photogenerated holes (h⁺), and sulfate radicals (SO₄•⁻) were discovered to be the main reactive species during PEC degradation. IBPA degradation and the formation of new compounds were verified using liquid chromatography-mass spectrometry. The *Lepidium sativum L* phytotoxicity test reveals that PEC-treated wastewater with IBPA exhibits decreased toxicity.

1. Introduction

Organic pollutants such as textile dyes, phenolic compounds, and antibiotics are typical persistent molecules that pose serious risks to the environment [1]. Especially pharmaceutical drugs are, in general, stable organic pollutants that remain in nature for a long time. A typical example is the anti-inflammatory drug 2-(4-isobutylphenyl)propanoic acid (IBPA), commonly found in aquatic and soil environments [2]. Bioaccumulation of IBPA poses a serious risk to ecosystems since it can result in biological deformities and microbial resistance [3]. Therefore, the development of highly efficient techniques for the removal of IBPA from wastewater is urgently needed. Photoelectrochemical (PEC)

methods have been demonstrated as effective advanced oxidation processes to decompose IBPA. According to the literature, PEC degradation of IBPA is mainly limited to the use of Na₂SO₄ and NaCl as electrolytes. After applying a sufficient voltage on the working electrode, in the presence of NaCl, reactive chlorine species (RCS) such as chlorine radicals (Cl•, Cl₂•⁻), chlorine (Cl₂), hypochlorite ion (ClO⁻), and hypochlorous acid (HOCl) that take part in IBPA degradation are produced [4–7]. However, when RCS reacts with the organics present in water, the degradation process may not always lead to complete mineralization, but instead toxic chlorination by-products are formed. Other reports where the main oxidant is the SO₄•⁻ radical, Na₂SO₄ electrolyte, have been found useful in the degradation of IBPA [8,9]. However, the

---

* Corresponding author.
E-mail address: saim.emin@ung.si (S. Emin).

relatively high standard oxidation potentials of SO_4^{2-} to $SO_4^{\cdot-}$ (2.60 V vs. NHE) present a drawback in the PEC oxidation of organic pollutants [10].

Recently, oxidation of organics using peroxymonosulfate (PMS) via non-radical and radical pathways has been investigated as a possible technique for water remediation [11–13]. The non-radical mechanism using PMS and a catalyst results in the oxidation of organic compounds and the formation of sulfate ions ($E^0(HSO_5^-/SO_4^{2-})$ = 1.75 V vs.NHE) [14,15]. On the other hand, PMS activation may proceed via the radical pathway, which may involve the formation of sulfate radical anions ($E^0(HSO_5^-/SO_4^{\cdot-})$ = 2.43 V vs.NHE) [16]. In the past, multiple approaches have been used to activate PMS to $SO_4^{\cdot-}$ species, such as ultrasonic irradiation [17], UV photolysis [18], photocatalysis (PC) [13,19–21], Fenton process [22], electrochemical (EC) [23], and PEC [24]. In the Fenton reactions, transition metal oxide catalysts such as Co_3O_4, Fe_3O_4, etc. have been proven as activators for PMS [25,26]. For example, cyclic transformation of the Fe^{3+}/Fe^{2+} redox couple in iron oxides allows efficient activation of PMS to generate $SO_4^{\cdot-}$ and/or •OH species [27]. However, leaching of hazardous metal ions (e.g., Co^{3+}) during the oxidation reaction can block practical applications for some of the catalysts used in the Fenton process [28]. Exploring alternative advanced oxidation processes such as PEC offers a safer way for PMS to be used in the degradation of organics.

Hematite (α-Fe_2O_3) with absorption in the visible range, band gap ($E_g \sim$ 1.9–2.2 eV) has been demonstrated as an efficient n-type semiconductor catalyst for PEC oxidation of water and degradation of organic pollutants [29,30]. Doping of α-Fe_2O_3 with different dopants such as Sn^{4+}, Si^{4+} and Ti^{4+} was discovered to be a successful method to improve light absorption, electrical conductivity, and reduce charge carrier recombination [31–33]. Especially, Sn^{4+} doping is attractive for modifying the optoelectronic properties of α-Fe_2O_3. It was demonstrated that Sn:Fe_2O_3 in the form of thin films shows improved PEC performance for different catalytic reactions due to the high charge-carrier density [34]. These studies also revealed that the Sn^{4+} self-doping of α-Fe_2O_3, during thermal treatments at elevated temperatures from the fluorine-doped tin oxide (FTO) substrate, also leads to improved photocurrent response [35]. In addition to element doping, oxygen vacancies (OVs) in metal oxides have been found to be useful tools to tune the activation of PMS for the degradation of organics, making their control highly desirable [36–38]. Recently, Wang et al. reported that N/C co-doped Fe_2O_3 showed promising PEC activity for the degradation of antibiotics using PMS [39]. To the best of our knowledge, there is a lack of research on PEC activation of PMS using α-Fe_2O_3 thin films for degradation of pharmaceutical drug pollutants.

Herein, we employed Sn:Fe_2O_3 thin films with controllable OVs as a catalyst for PEC water oxidation and degradation of IBPA in simulated wastewater solutions. The X-ray diffraction (XRD) and X-ray photoelectron spectroscopy (XPS) measurements confirmed the presence of OVs and Sn doping in Fe_2O_3 films. Furthermore, adjusting the concentration of Sn dopant allowed us to increase the PEC performance of α-Fe_2O_3 thin films. The improved PEC performance of Sn:Fe_2O_3 films was attributed to the higher carrier density and decreased charge transfer resistances, as revealed using electrochemical impedance spectroscopy (EIS) and Mott-Schottky (M−S) analyses. For the first time, Sn:Fe_2O_3 thin films were employed for efficient PEC degradation of IBPA using PMS as an activator. LC-MS was used to monitor the degradation of organics and their by-products. Phytotoxicity tests were carried out using *Lepidium sativum L* to evaluate the potential acute toxicity of untreated and PEC-treated IBPA water solutions.

2. Experimental details

2.1. Chemicals and materials

Furfuryl alcohol (FFA, 99%) was purchased from Fisher Scientific. Sodium sulfate (Na_2SO_4, >99%), sulfuric acid (H_2SO_4), sodium hydroxide (NaOH, 99%), ethylenediaminetetraacetic acid (EDTA), methanol (MeOH), and *tert*-butyl alcohol (TBA) were purchased from Sigma-Aldrich. 2-(4-isobutylphenyl)propanoic acid (IBPA, ≥98%), potassium peroxymonosulfate ($KHSO_5$, PMS) and coumarin (2H-1-benzopyran-2-one) were purchased from Alfa Aesar. 7-Hydroxycoumarin (7-HC) was obtained from Acros Organics. FTO on boroaluminosilicate glass (Solaronix, Swiss) was used as a substrate. A graphite block (99.9%) was purchased from Beijing Great Wall Co., Ltd. (China). Deionized water was used in all experiments.

2.2. Preparation of Sn:Fe₂O₃ thin films

Sn:Fe_2O_3 thin films were prepared by the spin-coating technique following the method developed by Machreki et al. [40]. In a typical procedure, Sn:Fe_2O_3 thin films with various OVs were obtained via an in-situ two-step annealing step at 750 °C for 5 min, followed by post-annealing (750 °C) at different times for 10, 30, and 60 min (in air) at an 8 °C min^{-1} heating rate.

2.3. Characterization of the Sn:Fe₂O₃ thin films

The XRD patterns were collected within the 2θ range from 10 to 90° with a constant step of 0.03° using a MiniFlex 600 W (Rigaku) diffractometer with Cu-K$_\alpha$ radiation. Phase identifications were performed with the PDXL software using the COD database. Diffuse reflectance spectra were recorded on a Lambda 650 UV–VIS spectrophotometer (PerkinElmer). The morphology of the Sn:Fe_2O_3 was studied using a scanning electron microscope, JSM 7100F SEM (JEOL) equipped with a field-emission electron gun (Oxford Instruments). Transmission electron microscopy (TEM) and scanning transmission electron microscope (STEM) studies were carried out with a JEOL 2100F. The XPS measurements were performed in the analysis chamber of the electron spectrometer ESCALAB-Mk II (VG Scientific) with a base pressure of ~5 × 10^{-8} Pa. The samples were mounted on a conductive adhesive tape, and C1s, O1s, Fe2p, Sn3d photoelectron, and TiLMM Auger spectra were recorded by using AlK$_\alpha$ radiation. All spectra were calibrated by using C 1s peak at 285.0 eV as a reference. The surface composition was evaluated from the photoelectron intensities divided by the corresponding photoionization cross sections taken from Scofield [2]. EC and PEC measurements were done in a three-electrode system with a Cappuccino cell [40]. An O-ring was used to define the electrode area at 0.283 cm^2. The potential of the working electrode was controlled by a potentiostat (EDAQ SP1). A graphite plate and a Hg/Hg_2SO_4 electrode were used as the counter and reference electrodes, respectively. Experimentally measured potentials were converted to the reversible hydrogen electrode (RHE) scale using the Nernst equation: $E_{RHE} = E_{Hg/Hg2SO4} + E°_{Hg/Hg2SO4} + 0.059 \times pH$. In this equation, $E_{Hg/Hg2SO4}$ was the measured potential against the Hg/Hg_2SO_4 reference electrode and $E°_{Hg/Hg2SO4}$ was taken as 0.65 V at 25 °C. The EIS of Sn:Fe_2O_3 thin films was studied under light in a 0.1 M Na_2SO_4 solution. The applied frequency ranged from 10 μHz to 1 MHz with an amplitude of 10 mV. The measured EIS data was fitted using the Zview software. The M−S studies were carried out in a three-electrode system in 0.1 M Na_2SO_4 solution (in the dark). Incident photon-to-current efficiency (IPCE) was obtained by measuring the photocurrent at 1.5 V vs. RHE in 0.1 M Na_2SO_4 solution (pH 5) under monochromatic light according to the following equation: $IPCE = (1240 \times j)/(\lambda \times P_{light})$ where, λ represents the incident light wavelength (nm), j is the photocurrent density of the film under specific incident light (mA/cm^2), and P_{light} is the used power density of monochromatic light (mW/cm^2).

2.4. PEC degradation of IBPA

PEC degradation of IBPA using Sn:Fe_2O_3 thin films was conducted in a two-compartment PEC cell comprising photoanodic (75 mL) and

cathodic (55 mL) chambers separated by a proton exchange membrane (Nafion-115) [40]. A three-electrode system was used during the PEC experiments, where the Sn:Fe$_2$O$_3$ thin film served as the working electrode (area 6 cm^2), Hg/Hg$_2$SO$_4$ electrode as the reference electrode, and a Pt plate as the counter electrode. We studied the degradation of IBPA (10 mg L^{-1}) in the presence of PMS (5 mM) as a supporting electrolyte at 25 °C with applied potential 1.5 V vs. RHE. The pH of the reaction solution was adjusted by adding 1 M H$_2$SO$_4$ and 1 M NaOH droplets. The PEC cell was illuminated by a visible LED during the reaction (7 cm away), but this did not result in sample heating. The incident light intensity of light (λ_{ex}, 400 nm, 6 mW cm^{-2}) was measured using an optical power meter (Thorlabs PM320E Dual-Channel Optical Power & Energy Meter Console). The IBPA degradation at different reaction times was monitored using a Perkin Elmer Lambda 25 UV–vis spectrophotometer. The degradation of intermediate products of IBPA during the PEC process was checked by LC-MS measurements using mass spectrometer Q-Tof Premier interfaced to the ultra-performance liquid chromatograph (UPLC) system based on Waters Acquity (Waters, Milford, USA). Phytotoxicity tests of organic solutions were carried out using *Lepidium sativum L.* Formation of •OH radicals were studied with a photoluminescence (PLS) spectrometer (FL920 spectrophotometer, Edinburgh Instruments) using a coumarin scavenger. LC-MS and phytotoxicity test conditions are provided in the Supplementary Information.

## 3. Results and discussion

3.1. Structural characterization

XRD patterns of the FTO substrate and Sn:Fe$_2$O$_3$ thin films deposited onto the FTO/glass are shown in Fig. 1. These intense diffraction peaks were indexed to the SnO$_2$ phase typical for tetragonal rutile structure (*P42/mnm*; PDF# 2101853). The diffraction peaks of the α-Fe$_2$O$_3$ sample treated for 10 min which appear at 32.95°, 35.35°, and 63.96° (2θ) correspond to the (1 0 4), (1 1 0), and (3 0 0) crystal planes of the hexagonal α-Fe$_2$O$_3$ (*R3c* (167); PDF# 21011692). Because of the high temperature heat treatment, Sn^{4+} in the FTO substrate can migrate into the α-Fe$_2$O$_3$ lattice, as previously reported [35,41]. With a substantial increase of Sn^{4+} doping level, a slight shift of the (1 1 0) peak to lower 2θ in the XRD patterns can be observed (Fig. S1). Usually, the greater cation sizes of Sn^{4+} (83 pm) compared to Fe^{3+} (78.5 pm) causes a lattice distortion. This trend could be associated with the incorporation of Sn at

the Fe lattice sites. Ling et al. have reported that Sn doping of α-Fe$_2$O$_3$ occurs predominantly at about 800 °C [42]. The effect of heat treatment time on crystal structure was recorded as shown in Fig. 1. An increase of the diffraction peak for the (3 0 0) crystal plane was observed for the α-Fe$_2$O$_3$ sample which was heat treated for 60 min. This indicates that the crystallinity in the α-Fe$_2$O$_3$ samples improves after heat treatment for a longer time.

Structural analysis of α-Fe$_2$O was achieved using TEM, as shown in Fig. 2a. The lattice spacing of 0.185 nm seen in the image can be assigned to the (0 2 4) crystal plane of hexagonal α-Fe$_2$O$_3$ (Fig. 2b). Selected area electron diffraction (SAED) pattern taken from the object in (a) shows that these particles are polycrystalline (Fig. 2c) [43]. The diffraction rings in the SAED pattern can be indexed to the (1 0 4), (1 1 0), (1 1 6), and (2 1 4) of α-Fe$_2$O$_3$. The uuniform distribution of Fe and O elements in the agglomerate (at. % ratio 2:3) can be seen in Fig. 2d, e as revealed using X-ray energy dispersive spectroscopy [40].

To estimate the film thickness and achieve better image contrast between the different phases, a SEM image was acquired using a back-scattered electron detector. Fig. 2f shows a cross-section view of the FTO/Sn:Fe$_2$O$_3$ electrode, where the FTO layer appears slightly brighter while the α-Fe$_2$O$_3$ layer on top of FTO is a little darker. The Sn:Fe$_2$O$_3$ film thickness was found to be about ~300 nm. The voids observed inside the Sn:Fe$_2$O$_3$ film are due to the Sn:Fe$_2$O$_3$ layers formed after two subsequent coatings (Fig. 2g-i). On the other hand, it is obvious that the heat treatment affects the morphology of the films [40,44].

To confirm the Sn^{4+} diffusion into the lattice of α-Fe$_2$O$_3$, XPS measurements were performed. The core level spectra of the Fe 2p, Sn 3d, and O 1s are shown in Fig. 3. The quantitative XPS data are listed in Table S1. The binding energies at 711.5 and 725 eV correspond to the Fe 2p$_{3/2}$ and Fe 2p$_{1/2}$ signals typical for Fe^{3+} ions. The associated satellite peak at 719.5 eV is due to the Fe^{3+} species found in both samples, abbreviated as 10 min and 30 min [45,46]. As shown in Fig. 3a, the peak intensity for the Fe^{3+} satellite decreased with the heat treatment time. With Sn doping, the intensity of the shakeup satellite decreases, indicating the appearance of Fe^{2+}. The calculated iron content of all samples from the XPS spectra is given in Table S1. It was found that the concentrations of iron taken from the Fe 2p$_{3/2}$ were about 35.88, 35.17, and 26.12 at. % in the samples at 10, 30, and 60 min, respectively. The Sn detected in the α-Fe$_2$O$_3$ thin films annealed at 750 °C was found to
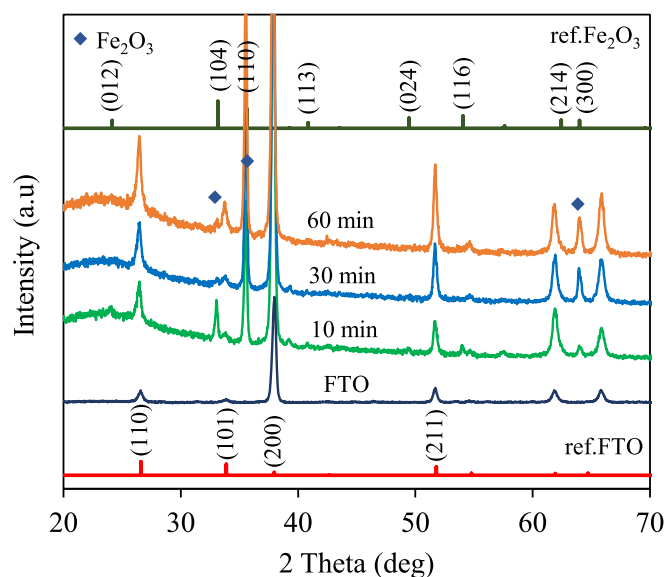
Fig. 1. XRD patterns of FTO (F: SnO$_2$) and α-Fe$_2$O$_3$ coated on FTO substrates at different annealing times at 750 ºC.
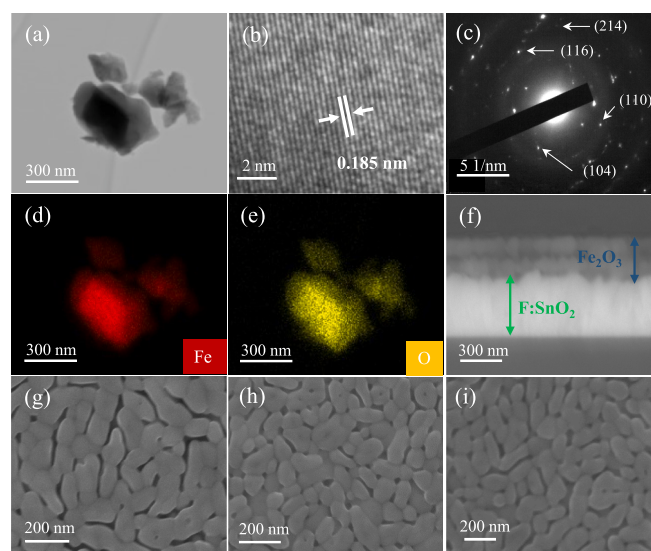
Fig. 2. (a) Bright-field STEM image of α-Fe$_2$O$_3$ and its corresponding element maps of (d) Fe and (e) O. (b) HR-TEM image of Sn-Fe$_2$O$_3$ lattice, and (c) SAED pattern taken from (a) in TEM mode. (f) Cross-section of the α-Fe$_2$O$_3$ thin film. SEM images taken in top-view from the Sn:Fe$_2$O$_3$ thin film at different heat treatment times: (g) 10 min, (h) 30 min, and (i) 60 min.
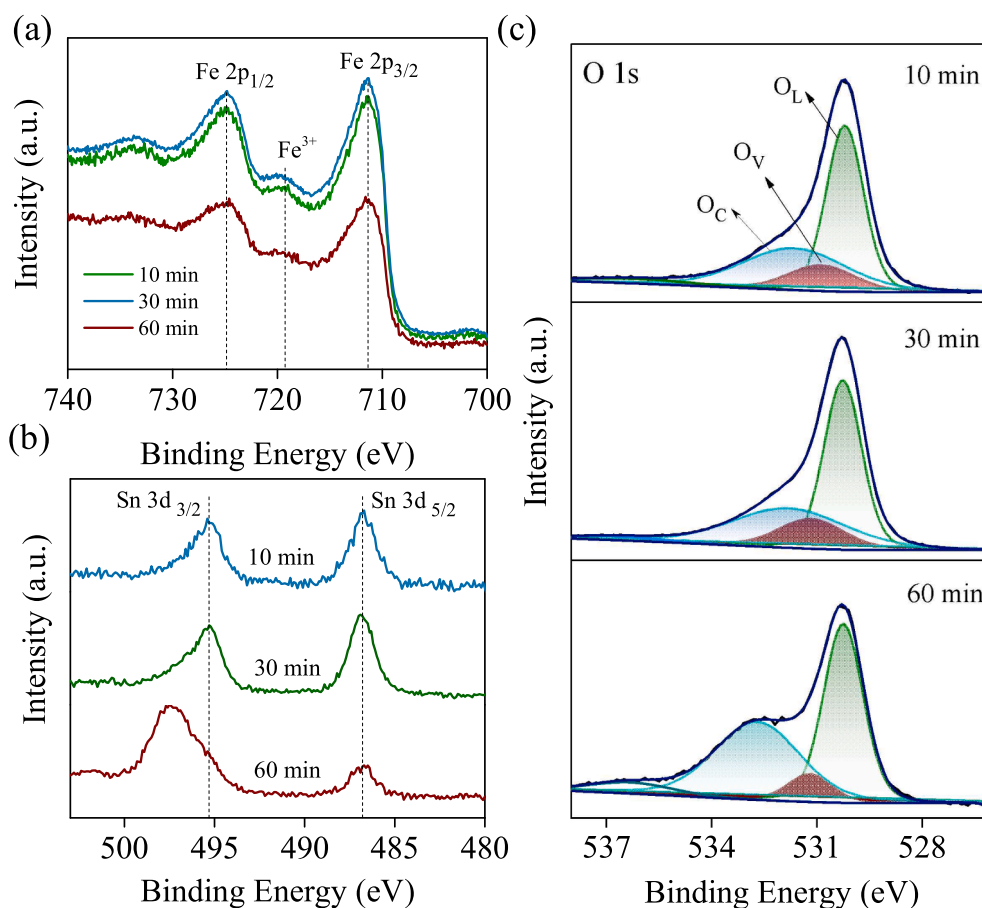
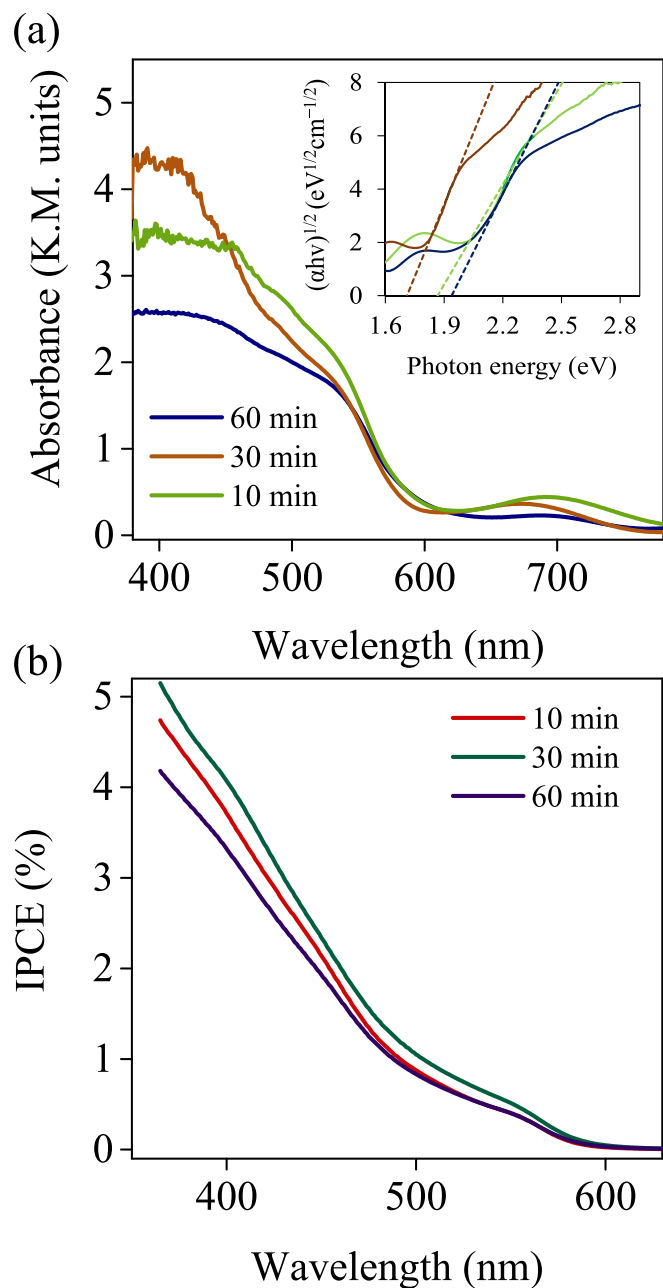**Fig. 3.** XPS spectra of Sn:Fe_2O_3 at different heat treatment times: (a) Fe 2p, (b) Sn 3d, and (c) O 1s.

originate from the FTO substrates, as reported previously [34,35]. The signals at 495.2 and 486.8 eV correspond to the Sn $3d_{3/2}$ and Sn $3d_{5/2}$ peaks, respectively (Fig. 3b). The Sn 3d peaks are associated with the Sn^{4+} chemical state found typically in SnO_2 [47]. The Sn $3d_{5/2}$ (486.8 eV) has a binding energy between SnO_2 (487.2 eV) and SnO (486.3 e V) [48,49]. The lower binding energy peak is attributed to the Sn being incorporated into the FeO matrix. This is consistent with the expected binding energy shifts because the electronegativity of Sn (1.96) is higher than that of Fe (1.83) [41,49,50]. These unintentionally Sn doped Fe_2O_3 samples show decreasing atomic concentrations (%) for Sn with heat treatment time. The α-Fe_2O_3 annealed for 10 min has the maximum Sn doping amount, which is equal to 0.79 at. % (Table S1). Further, the Sn $3d_{3/2}$ peak of the sample heated for 60 min slightly shifts toward higher binding energies (Fig. 3b). The shift could be associated with the formation of SnO_2 clusters on the Fe_2O_3 surface. The XRD studies also supports since there is an increase in (1 0 1) plane intensity of SnO_2.

The XPS spectra of O 1s core level revealed the presence of OVs as shown in Fig. 3c. The broad O 1s peak is composed of different signals indicated as O_L, O_C, and O_V [51]. The Fe–O bond (O_L) in α-Fe_2O_3 appear at low binding energy like 530.22 eV [52]. The middle band corresponds to the OVs (O_V), which is centered at 531.15 eV [53]. Chemisorbed oxygen (O_C) signal has the greatest binding energy which appears at 531.68 eV [49]. The area ratio of the O_V peak to all O 1s signals was calculated using this formula: (O_V / (O_L + O_V + O_C)) [52]. The area of the O_V sample treated after 10 min is equal to 13.8%, 30 min is 14.9% and at 60 min it drops to 7.7%. Heating for 30 min can result in reasonably high oxygen vacancy density, which has been shown to be favorable for increasing PEC efficiency [50]. The introduction of Sn^{4+} dopant causes the replacement of certain iron atoms with tin atoms, creating defects in the Sn_{Fe+} site. Additionally, the positive charge of the

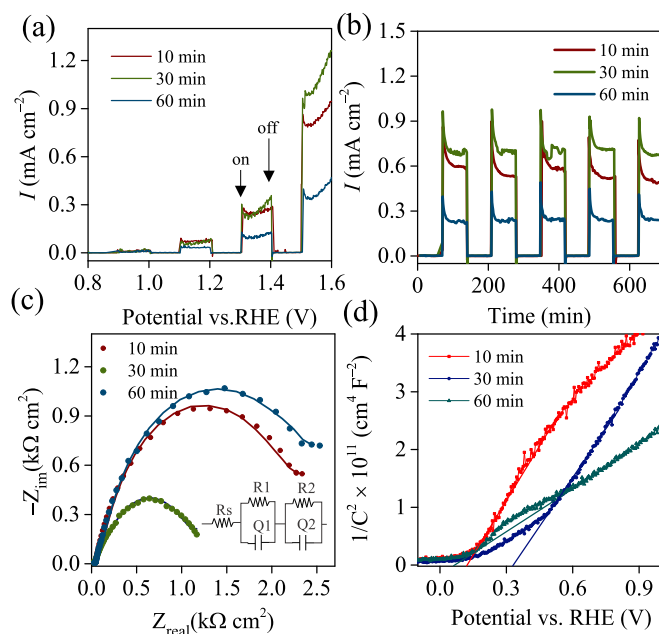Sn_{Fe+} traps the oxygen electron cloud, increasing the binding energy for the O 1s peak [52,54].

Fig. 4a shows the absorption spectra of Sn:Fe_2O_3 thin films. The observed difference in the absorbance of α-Fe_2O_3 is most likely attributed to the Sn doping and morphological changes seen in the SEM images. The electron transition from the VB to the CB (O 2p → Fe 3d) causes an increase in absorbance at wavelengths shorter than 600 nm [55,56]. The E_g of the α-Fe_2O_3 film was determined using the Tauc equation and assuming an indirect transition. The E_g value taken from the intercept is equal to ~1.88 eV (10 min), 1.75 eV (30 min), and 2.0, eV (60 min) (inset in Fig. 4a). This value matches the E_g of α-Fe_2O_3 reported in the literature [40,57,58]. IPCE measurements were used to evaluate the quantum efficiency of these three different photoanodes. As shown in Fig. 4b, the Sn:Fe_2O_3 heated for 30 min exhibits the highest IPCE value, which is obviously higher than the Sn:Fe_2O_3 films annealed at 10 min and 60 min. The IPCE values of all three photoanodes decrease close to zero at wavelengths above 600 nm, indicating a lack of light absorption above this range [59]. The IPCE results are in good agreement with UV–vis data, demonstrating that the improved PEC activity of Sn:Fe_2O_3 is from a light-driven water oxidation reaction.

The PEC water oxidation activities of the Sn:Fe_2O_3 films were studied both in acid (0.1 M Na_2SO_4, pH 5) and alkaline media (1 M KOH, pH 13.9). The Sn:Fe_2O_3 sample treated for 30 min shows the highest PEC activity, as given in Fig. 5a and Fig. S2. Notably, the photocurrent density of the sample treated at 30 min is three times that of the sample treated at 60 min. However, the photocurrent density decreased after 60 min of treatment due to the lower concentrations of OVs, Sn, and Fe (as shown in Table S1). It was found that the concentration of Sn taken from the Sn $3d_{5/2}$ decreased from 0.79% to 0.55%, OVs from 9.3% to 4.8% and for Fe from 35.8% to 26.1%. The photocurrent difference between

(a)

Fig. 4. (a) Absorbance spectrum of Sn:Fe$_2$O$_3$ thin film at different heat treatment times. The inset is a Tauc plot. (b) IPCE of Sn:Fe$_2$O$_3$ samples recorded under a bias of 1.5 V vs. RHE in 0.1 M Na$_2$SO$_4$ (pH 5).

Fig. 5. (a) LSV of Sn:Fe$_2$O$_3$ in 0.1 M Na$_2$SO$_4$ (pH 5) recorded at 5 mV/s under chopped illumination (400 nm). Samples are annealed at different times (b) Current vs. time recorded at 1.5 V vs. RHE. (c) Nyquist plot at 1.23 V vs. RHE under illumination. (d) M–S plots measured in 0.1 M Na$_2$SO$_4$ at 5 kHz.

the treated α-Fe$_2$O$_3$ films at various times may be read as evidence that the quantity of OVs in the α-Fe$_2$O$_3$ film clearly affect its photocurrent response property (Fig. 3) [45,46,60]. On the other hand, Annamalai et al. reported a sudden drop of photocurrent in hematite nanorods heated at high temperatures. In their case, the drop was ascribed to the conductivity losses in the FTO substrate [61]. In addition to the drop in conductivity, the decrease in the photocurrent density at a particular Sn concentration is also correlated with the narrowing of the space charge layer in semiconductors. The low Sn dopant levels at 60 min perhaps causes a decrease in the photogenerated holes that reduce the migration of holes towards the hematite-liquid junction to perform water oxidation. Further, the stability of the three films was studied by recording the photocurrent at an applied bias of 1.5 V vs. RHE. The three samples exhibited good stability (Fig. 5b). In the dark (OFF), the current values were almost zero, while under illumination (ON), the photocurrent

rapidly increased to a steady state value. This trend was reproducible for several light on/off cycles, where the photocurrent of the sample treated for 30 min reaches 0.8 mA cm^{-2} at 1.5 V vs. RHE.

To check the kinetic difference between the three films during water oxidation, EIS studies were investigated at an applied potential of 1.23 V vs. RHE under illumination (Fig. 5c). After fitting the EIS data with an appropriate equivalent circuit, the charge transfer resistance was obtained. The resistance values are found to be 52, 22, and 72 Ω for the Sn:Fe$_2$O$_3$ samples, abbreviated as 10 min, 30 min, and 60 min, respectively. The lowest charge transfer of Sn:Fe$_2$O$_3$ film treated for 30 min explains its profound PEC activity [40]. The lower resistance could be linked to the higher concentration of OVs. It is widely accepted that higher oxygen vacancy levels lead to a rise in carrier density, which in turn facilitates easier electron transfer.

The PEC performance of Sn:Fe$_2$O$_3$ samples were further characterized using M–S plots. It was found that these films exhibit an *n*-type conductivity due to the positive slope recorded in the M–S plots (Fig. 5d and Fig. S3) [60]. Extrapolating the linear region of the M–S curve and reading the intercept value on the abscissa gives the V_{FB}. The obtained V_{FB} values of Sn:Fe$_2$O$_3$ film treated for 10, 30, and 60 min samples are shown in Table S2, which are close to the literature reported values [40]. The observed shift in V_{FB} potential may also be a factor contributing to the improved PEC activity [61,62]. Due to the presence of surface oxygen vacancies, the charge carrier concentration of the Sn:Fe$_2$O$_3$ – 30 min film significantly increases comparing to Sn:Fe$_2$O$_3$ – 60 min, which can facilitate the charge transfer process. Therefore, the survival period of holes can be effectively extended, and the charge carriers' recombination is reduced [21]. The donor density (N_D) values were determined from the slope of the M–S plot at 5 kHz. The N_D value of the Sn:Fe$_2$O$_3$ film treated at 30 min was calculated to be 3.1×10^{20} cm^{-3}, which is higher than the N_D of the sample treated at 10 min (2.5×10^{20} cm^{-3}) and 60 min (1.9×10^{20} cm^{-3}) [44]. As a rule, high N_D is associated with improved charge transport which in turn may result in better PEC activity [40,50].

According to related reports, the OVs can generate new intermediate defect levels [21,63]. The photogenerated electrons can not only jump from VB to defective energy levels, but they can also be further

stimulated from defective energy levels to CB, which may also contribute to the decrease in band gap. After creation of OVs, the photo response is extended as shown in Fig. 4a. The OVs can promote charge transfer by inhibiting photogenerated electron–holes recombination. The reason is that the photogenerated electrons preferentially enter the OVs instead of recombining with holes [64–66]. In the present study, the presence of OVs in Sn:Fe$_2$O$_3$ improves photocurrent significantly.

3.2. PEC oxidation of IBPA using PMS

We used IBPA as a model pollutant in PEC degradation studies. The absorption spectra of IBPA in 5 mM PMS solution at various PEC degradation intervals are given in Fig. 6a. Because of the higher PEC water oxidation activity, the Sn:Fe$_2$O$_3$ – 30 min film was used as a model photoanode (Fig. 6b). Furthermore, the degradation of IBPA was also tested using other methods: EC, PC, and PL (Fig. 6c). The fastest degradation is achieved using PEC. Complete degradation of 10 mg L^{-1} of IBPA was observed after 210 min using PEC. On the other hand, the EC, PC, and photolysis (PL) methods removed just 18, 20, and 16 % of the IBPA, respectively. The IBPA degradation follows a pseudo first-order kinetics. The highest rate constant of IBPA degradation was achieved using PEC using optimum PMS level (Fig. 6d). In comparison to literature reports for PEC degradation of IBPA, Gomes et al. have shown that Zn-TiO$_2$ catalysts yielded lower rate constants (e.g., $k_1 = 0.0008$ min^{-1}) using Na$_2$SO$_4$ [9]. Several studies reported PEC degradation of IBPA using Cl$^-$ ions too [4–7]. However, in the presence of Cl$^-$ under UV–visible-light, toxic chlorinated by-products such as ClO$_3^-$ and ClO$_4^-$ are produced [62].

3.3. Impact of operating parameters

The influence of pH on IBPA degradation was studied in the pH interval from 3 to 9. The degradation rate of IBPA was faster in acidic media than in neutral or alkaline media (Fig. 7a). The PEC degradation was 99%, 30%, and 41% at pH 3, 6, and 9. The higher PEC activity at lower pH may be attributed to the following reasons [61] (i) the semiconductor flat-band potential or (ii) the ability to efficiently generate

Fig. 6. (a) Absorption spectra of IBPA (10 mg L^{-1}) recorded during the PEC experiment using Sn:Fe$_2$O$_3$–30 min. (b) Comparison of IBPA degradation efficiency activated by 5 mM PMS using three different films of Sn:Fe$_2$O$_3$, pH 3. (c) Normalized concentration (C/C_0) of IBPA vs. time for EC, PC, PL, and PEC in the presence of 5 mM PMS, pH 3. (d) Average reaction rate constant (min^{-1}) for degradation of IBPA.

SO$_4^{\bullet-}$. It is known that in acidic medium, SO$_4^{\bullet-}$ is the primary reactive species due to their higher redox potential (2.5–3.1 V vs. NHE) compared with $^\bullet$OH (1.8–2.7 V vs. NHE) [10].
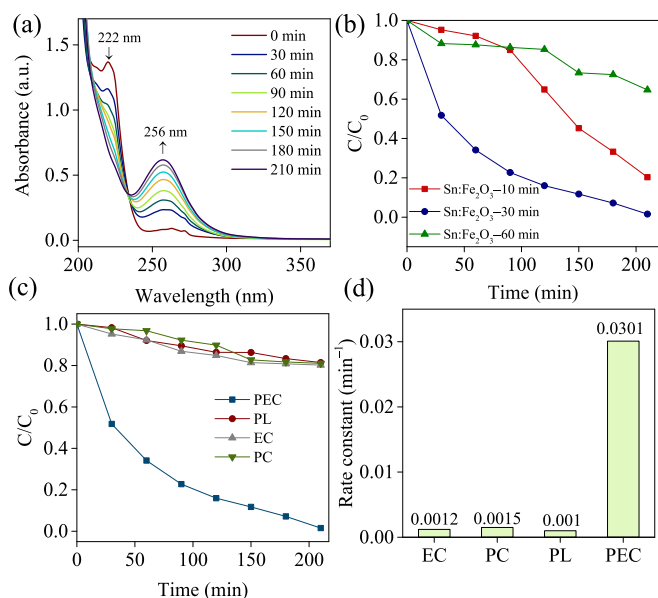
Previous studies have demonstrated that inorganic anions have apparent influence on the performance of oxidation processes [29,67]. Inorganics anions such as NO$_3^-$, HCO$_3^-$ and HPO$_4^{2-}$ are primary constituents in water systems. The effect of these anions on PEC degradation of IBPA using Sn:Fe$_2$O$_3$ – 30 min thin film were also investigated. As shown in Fig. S4a, NO$_3^-$ exerted an insignificant effect on IBPA degradation. In similar way, HCO$_3^-$ showed a negligible inhibitory effect [68], indicated by a little decrease in IBPA degradation. On the other side, HPO$_4^{2-}$ which has a strong binding affinity towards iron oxides, was also investigated [68]. The addition of 10 mM phosphate ions led to a sharp decrease in the PEC degradation of IBPA. The inhibition caused by HPO$_4^{2-}$ should be due to its adsorption on the active sites of the catalyst.

The degradation of IBPA was also tested on two kinds of water samples (Fig. S3b). The quality indicator of commercial mineral water (Radenska - Radenci spring, Slovenia) was listed in Table S3. The degradation rates of IBPA in mineral water, and deionized water were 0.229, and 0.301 min^{-1}, respectively. These similar degradation rates demonstrate that the PEC degradation of IBPA using PMS is effective in real waters.
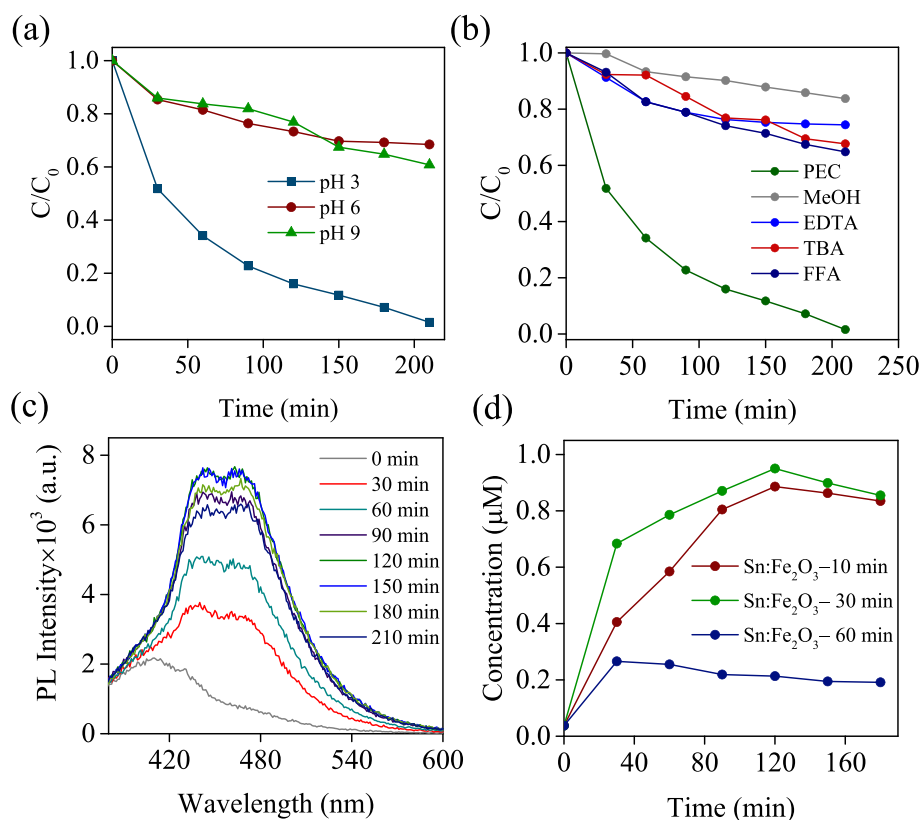
3.4. Reaction mechanisms of the PEC process

Controlled studies were used to identify the primary active species during the degradation of IBPA to reveal the mechanism of PEC degradation. Different molecules were used in the tests, such as scavengers like EDTA for the photogenerated holes (h$^+$), TBA for the $^\bullet$OH radicals, FFA for the singlet oxygen (^{1}O$_2$), and MeOH for the SO$_4^{\bullet-}$/$^\bullet$OH radicals (Fig. 7b) [25,69,70]. In the presence of EDTA, the degradation of IBPA was slow, which indicated that the photogenerated holes produced in the Sn:Fe$_2$O$_3$ were suppressed. Adding in the solution of a TBA scavenger was found to inhibit the generation of $^\bullet$OH radicals, which in turns lower the degradation efficiency. Moreover, to check the formation of SO$_4^{\bullet-}$ and $^\bullet$OH during the degradation of IBPA in 5 mM PMS, MeOH was used as a scavenger [71]. In this case, the IBPA degradation was negligible, indicating that that both SO$_4^{\bullet-}$ and $^\bullet$OH contribute toward the degradation of IBPA. The activator PMS traps electrons and produces SO$_4^{\bullet-}$ species, which are expected to cause degradation of IBPA. On the other hand, the FFA scavenger blocks the degradation of IBPA which indicates that singlet oxygen (^{1}O$_2$) was produced. It is well-known that ^{1}O$_2$ species play a major role in the degradation of organics. Therefore, we expect that ^{1}O$_2$ also causes a smaller level of BPA degradation (Fig. 7b). To get an estimate of the photogenerated $^\bullet$OH species, coumarin was used as a quantitative probe [72]. Hydroxylated coumarin (e.g., 7-HC) is formed in the reaction between coumarin and $^\bullet$OH radical. To determine the amount of formed 7-HC a standard calibration plot was built by recording the PLS intensity of 7-HC compound at different concentrations (Fig. S4a, b) [73]. The PEC experiments were performed using a coumarin (4 × 10^{-5} M) aqueous solution. The variations in the PLS spectra of a coumarin solution during PEC treatment are shown in Fig. 7c. It was possible to detect a progressive increase in the emission intensity of the 7-HC at around 455 nm. The generated 7-HC at the Sn:Fe$_2$O$_3$ (treated for 30 min) surface follows zero-order reaction rate kinetics. Fig. 7d shows plots of produced 7-HC (e.g., $^\bullet$OH) vs. illumination time, which indicate that the Sn:Fe$_2$O$_3$ thin film exhibited the fastest formation rate of $^\bullet$OH (0.028 μM min^{-1}) compared with the other films, Sn:Fe$_2$O$_3$–10 min (0.018 μM min^{-1}) and Sn:Fe$_2$O$_3$–60 min (0.005 μM min^{-1}). It is evident that all proposed species take part in the degradation of IBPA, with a more pronounced effect caused by SO$_4^{\bullet-}$ and $^\bullet$OH radicals.

To prove the degradation efficiency and mineralization of IBPA, LC-MS was used to check the formation of any by-products during PEC degradation. Fig. S6 shows a typical chromatogram of IBPA recorded at different PEC times. The complete disappearance of the IBPA peak (5.5

Fig. 7. Normalized IBPA concentration vs. time recorded using Sn:Fe$_2$O$_3$–30 min during PEC degradation in 5 mM PMS (N$_2$ bubbling; pH 3) under an applied 1.5 V vs. RHE at (a) different pH values and (b) different scavengers: 0.1 M FFA, 0.1 M TBA, 0.01 M EDTA, and 0.1 M MeOH. (c) Emission spectra of 40 μM coumarin solution in 5 mM PMS at different PEC treatment times. (d) Plots of 7-HC concentration produced at different PEC treatment times using three different films.

min elution) occurs at 210 min irradiation time. During the degradation of IBPA, a new compound is detected that is structurally different from the parent molecule. The peak at 3.4 min elution time may be due to the formation of new C–O bonds, promoted by the attack of strong oxidant species, at the anode surface [74]. Quintana et al. identified a similar molecule containing the group –COCOOH in the meta position after the IBPA degradation. It is evident that IBPA reacts with a radical species (photogenerated holes, ^{1}O$_2$, SO$_4^{\cdot-}$, and $^\cdot$OH) to produce 3-(4-hydroxyphenyl)propionic acid, which subsequently undergoes mineralization [75]. According to the experimental results mentioned above, a possible mechanism could be proposed for PEC degradation of IBPA using Sn: Fe$_2$O$_3$ –30 min in the presence of PMS. It is worth noting that Sn doping has significantly increased the role of OVs in Sn:Fe$_2$O$_3$/PMS system. There are several possible pathways for degradation of IBPA during PEC. Firstly, photogenerated electrons and holes in Sn:Fe$_2$O$_3$ (Eq. (1)) are consumed by PMS, leading to the generation of SO$_4^{\cdot-}$ and SO$_5^{\cdot-}$ radicals according to Eq. (2) and Eq. (3). (Eq. (4)) [76,77].

$$Fe_2O_3 + h\nu \rightarrow Fe_2O_3(h + e^-) \tag{1}$$

$$HSO_5^- + e^- \rightarrow SO_4^{\cdot-} + OH^- \tag{2}$$

$$HSO_5^- + h^+ \rightarrow SO_5^{\cdot-} + H^+ \tag{3}$$

$$SO_5^{\cdot-} + SO_5^{\cdot-} \rightarrow 2SO_4^{\cdot-} + O_2 \tag{4}$$

The reaction of SO$_4^{\cdot-}$ radicals [21], with water, may give SO$_4^{2-}$, H$^+$, and $^\cdot$OH species Eq. (5)–(8) [71].

$$Fe^{3+} + HSO_5^- \rightarrow Fe^{2+} + SO_5^{\cdot-} + H^+ \tag{5}$$

$$Fe^{2+} + HSO_5^- \rightarrow Fe^{3+} + SO_4^{\cdot-} + OH^- \tag{6}$$

$$SO_4^{\cdot-} + H_2O \rightarrow SO_4^{2-} + {}^\cdot OH + H^+ \tag{7}$$

$$SO_4^{\cdot-} + OH^- \rightarrow SO_4^{2-} + {}^\cdot OH \tag{8}$$

There is also a possible second pathway for the generation of reactive species that involves OVs. The latter is converted to active oxygen (O*). Further, O* is transformed into singlet oxygen (^{1}O$_2$) in the presence of PMS, shown in the following equations [39]:

$$O_v \rightarrow O^* \tag{9}$$

$$O^* + HSO_5^- \rightarrow HSO_4^- + {}^1O_2 \tag{10}$$

The hypothesis above was checked by using PMS in an inert N$_2$ atmosphere during IBPA degradation. Negligible variations in the IBPA degradation were observed, which indicates that ^{1}O$_2$ originated from the lattice oxygens in the Sn:Fe$_2$O$_3$ photoanode rather than from dissolved oxygen in the solution (Fig. 7b) [26]. Similar results have been found for Ca-doped Fe$_2$O$_3$ and Co-doped TiO$_2$ systems [16,39]. It was concluded that the OVs in Sn:Fe$_2$O$_3$ can enhance the production of ^{1}O$_2$, SO$_4^{\cdot-}$ and $^\cdot$OH, which cause PEC degradation of IBPA.

3.5. Reusability test

The reusability test of the Sn:Fe$_2$O$_3$–30 min electrode was evaluated by carrying out repeated PEC cycles of IBPA degradation under visible light (Fig. 8). The film showed over 90% degradation efficiency for IBPA in each cycle. It seems that the OVs in Sn:Fe$_2$O$_3$–30 min facilitate the efficient activation of PMS. These results show that the Sn:Fe$_2$O$_3$–30 min photoanode is stable against corrosion and could be reused in PEC studies.
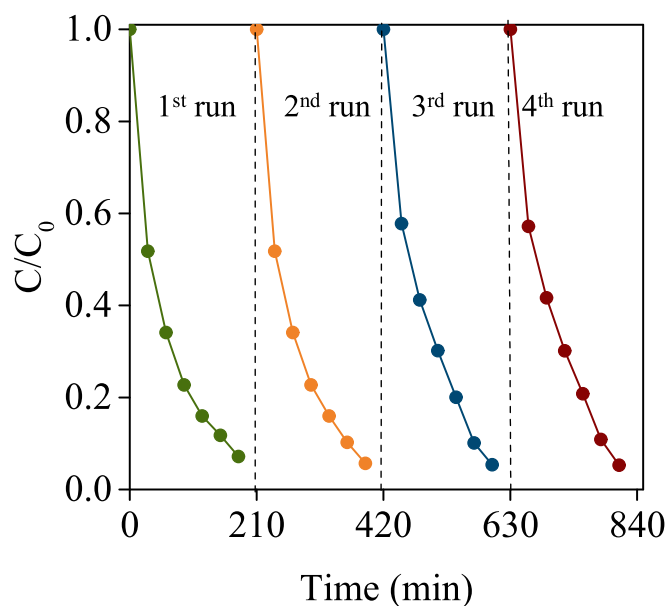
Fig. 8. PEC degradation of IBPA in 5 mM PMS for four runs at 1.5 V vs. RHE.

3.6. Phytotoxicity test using Lepidium sativum L.

Seed germination and root growth of *L. sativum* were carried out to study the phytotoxic effect of tested IBPA solutions (Fig. S7). Inhibition (%) values are from 47 and −3.6% for the untreated and PEC treated IBPA solutions, respectively. The descent in the inhibition value shows that the toxicity caused by IBPA decreased after PEC treatment. Table S4 provides the relative germination percentage (RGP) and relative radicle growth (RRG) values that were used to calculate the germination index (GI) values of the untreated and PEC treated IBPA samples. The treated water solutions give higher values for RGP, RRG, and GI, which are considered beneficial of plant growth [40]. According to Zucconi et al. [78] phytotoxicity is classified depending on the GI value: a GI value of 80% shows that the pollutant present is not phytotoxic. A GI value higher than 100% indicates a plant–stimulating effect (Fig. 9). In our case, the GI determined after 3 h PEC treatment is above 90% which means that at the studied concentration ([IBPA] = 10 mg L^{-1}) there is an absence of phytotoxicity [79]. The trend in phytotoxicity demonstrates that PEC treatment improves water quality.

4. Conclusions

Porous Sn:Fe$_2$O$_3$ thin films have been prepared using spin-coating and subsequent heat-treatment at elevated temperatures. The PEC performance of α-Fe$_2$O$_3$ thin films was modulated by adjusting the Sn dopant level (e.g., OVs) in the metal oxide. The Sn:Fe$_2$O$_3$–30 min thin films demonstrated the best photocurrent density due to the increase of carrier density. Detailed photo-electrochemical analyses of the α-Fe$_2$O$_3$ electrode were performed using techniques like flat-band measurements, EIS, LSV, and IPCE. For the first time, Sn doped Fe$_2$O$_3$ thin films were used for efficient PEC degradation of IBPA using PMS as an activator. The degradation efficiency of IBPA reached 99% for the Sn:Fe$_2$O$_3$–30 min photoanode, which was much higher than other films. The key reactive species during PEC degradation were found to be the photogenerated holes, $^1O_2$, $SO_4^{\cdot-}$, and ·OH, as evident from free radical quenching experiments. The complete degradation of IBPA was confirmed using LC-MS analysis. A phytotoxicity test with *Lepidium sativum L* showed that IBPA toxicity was significantly reduced after PEC treatment. PEC treated water offers higher values for RGP, RRG, and GI, which are all indicators for plant growth. This work provided a new perspective on designing efficient PEC systems for environmental wastewater remediation.
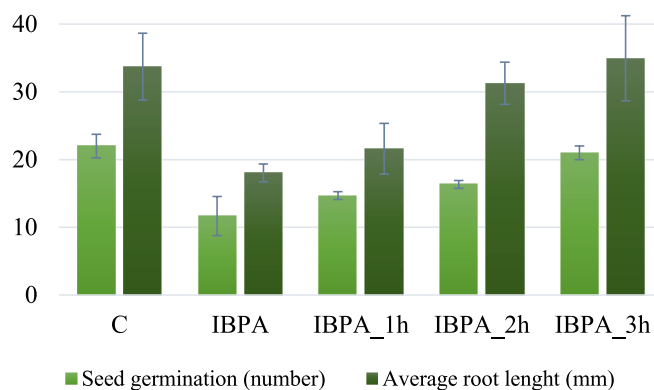

Fig. 9. Seed germination test for toxicity analysis of IBPA solutions.

CRediT authorship contribution statement

Manel Machreki: Writing – original draft, Visualization, Methodology, Investigation, Formal analysis, Data curation. **Georgi Tyuliev:** Formal analysis, Data curation. **Dušan Žigon:** Formal analysis, Data curation. **Qian Guo:** Formal analysis, Data curation. **Takwa Chouki:** Formal analysis, Data curation. **Ana Belén Jorge Sobrido:** Formal analysis, Visualization, Investigation. **Stoichko Dimitrov:** Visualization, Investigation. **Saim Emin:** Conceptualization, Investigation, Project administration, Funding acquisition, Methodology, Supervision, Validation, Visualization.

Declaration of Competing Interest

The authors declare that they have no known competing financial interests or personal relationships that could have appeared to influence the work reported in this paper.

Data availability

No data was used for the research described in the article.

Appendix A. Supplementary data

Supplementary data to this article can be found online at https://doi.org/10.1016/j.jphotochem.2023.115126.

References

[1] Z. Ren, H. Romar, T. Varila, X. Xu, Z. Wang, M. Sillanpää, T. Leiviskä, Ibuprofen degradation using a Co-doped carbon matrix derived from peat as a peroxymonosulphate activator, Environ. Res. 193 (2021), https://doi.org/10.1016/j.envres.2020.110564.

[2] M. Ma, L. Chen, J. Zhao, W. Liu, H. Ji, Efficient activation of peroxymonosulfate by hollow cobalt hydroxide for degradation of ibuprofen and theoretical study, Chinese Chem. Lett. 30 (2019) 2191–2195, https://doi.org/10.1016/j.cclet.2019.09.031.

[3] G. Zhang, Y. Ding, W. Nie, H. Tang, Efficient degradation of drug ibuprofen through catalytic activation of peroxymonosulfate by Fe$_3$C embedded on carbon, J. Environ. Sci. (China) 78 (2019) 1–12, https://doi.org/10.1016/j. jes.2018.10.002.

[4] Q. Sun, Y.P. Peng, H. Chen, K.L. Chang, Y.N. Qiu, S.W. Lai, Photoelectrochemical oxidation of ibuprofen via Cu$_2$O-doped TiO$_2$ nanotube arrays, J. Hazard. Mater. 319 (2016) 121–129, https://doi.org/10.1016/j.jhazmat.2016.02.078.

[5] H. Chen, Y.P. Peng, T.Y. Chen, K.F. Chen, K.L. Chang, Z. Dang, G.N. Lu, H. He, Enhanced photoelectrochemical degradation of Ibuprofen and generation of hydrogen via BiOI-deposited TiO$_2$ nanotube arrays, Sci. Total Environ. 633 (2018) 1198–1205, https://doi.org/10.1016/j.scitotenv.2018.03.268.

[6] K.L. Chang, Q. Sun, Y.P. Peng, S.W. Lai, M. Sung, C.Y. Huang, H.W. Kuo, J. Sun, Y. C. Lin, Cu$_2$O loaded titanate nanotube arrays for simultaneously photoelectrochemical ibuprofen oxidation and hydrogen generation, Chemosphere 150 (2016) 605–614, https://doi.org/10.1016/j.chemosphere.2016.02.016.

[7] Y.P. Peng, C.C. Liu, K.F. Chen, C.P. Huang, C.H. Chen, Green synthesis of nano-silver–titanium nanotube array (Ag/TNA) composite for concurrent ibuprofen degradation and hydrogen generation, Chemosphere 264 (2021), 128407, https://doi.org/10.1016/j.chemosphere.2020.128407.

[8] X. Zhao, J. Qu, H. Liu, Z. Qiang, R. Liu, C. Hu, Photoelectrochemical degradation of anti-inflammatory pharmaceuticals at Bi$_2$MoO$_6$-boron-doped diamond hybrid electrode under visible light irradiation, Appl. Catal. B Environ. 91 (2009) 539–545, https://doi.org/10.1016/j.apcatb.2009.06.025.

[9] A. Gomes, T. Frade, K. Lobato, M.E.M. Jorge, M.I. Da Silva Pereira, L. Ciriaco, A. Lopes, Annealed Ti/Zn–TiO$_2$ nanocomposites tested as photoanodes for the degradation of Ibuprofen, J. Solid State Electrochem. 16 (2012) 2061–2069, https://doi.org/10.1007/s10008-011-1608-0.

[10] E. Kusmierek, Semiconductor electrode materials applied in photoelectrocatalytic wastewater treatment−an overview, Catalysts 10 (2020) 439, https://doi.org/10.3390/catal10040439.

[11] J. Liao, D.-Y. Kwak, F. Sieland, C. Kim, D.W. Bahnemann, W. Choi, Visible light-induced catalytic activation of peroxymonosulfate using heterogeneous surface complexes of amino acids on TiO$_2$, Appl. Catal. B Environ. 225 (2018) 406–414.

[12] A. Rastogi, S.R. Al-Abed, D.D. Dionysiou, Sulfate radical-based ferrous-peroxymonosulfate oxidative system for PCBs degradation in aqueous and sediment systems, Appl. Catal. B Environ. 85 (2009) 171–179, https://doi.org/10.1016/j.apcatb.2008.07.010.

[13] J. Lim, M.R. Hoffmann, Peroxymonosulfate (PMS) activation on cobalt-doped TiO2 nanotubes: degradation of organics under dark and solar light irradiation conditions, Environ. Sci. Nano 7 (2020) 1602–1611, https://doi.org/10.1039/d0en00131g.

[14] X. Duan, H. Sun, Y. Wang, J. Kang, S. Wang, N-doping-induced nonradical reaction on single-walled carbon nanotubes for catalytic phenol oxidation, ACS Catal. 5 (2015) 553–559, https://doi.org/10.1021/cs5017613.

[15] H. Sun, S. Liu, G. Zhou, H.M. Ang, M.O. Tadé, S. Wang, Reduced graphene oxide for catalytic oxidation of aqueous organic pollutants, ACS Appl. Mater. Interfaces 4 (2012) 5466–5471, https://doi.org/10.1021/am301372d.

[16] J. Lim, Y. Yang, M.R. Hoffmann, Activation of Peroxymonosulfate by Oxygen Vacancies-Enriched Cobalt-Doped Black TiO$_2$ Nanotubes for the Removal of Organic Pollutants, Environ. Sci. Tech. 53 (2019) 6972–6980, https://doi.org/10.1021/acs.est.9b01449.

[17] R. Yin, W. Guo, H. Wang, J. Du, X. Zhou, Q. Wu, H. Zheng, J. Chang, N. Ren, Enhanced peroxymonosulfate activation for sulfamethazine degradation by ultrasound irradiation: Performances and mechanisms, Chem. Eng. J. 335 (2018) 145–153, https://doi.org/10.1016/j.cej.2017.10.063.

[18] X. Ao, W. Liu, W. Sun, M. Cai, Z. Ye, C. Yang, Z. Lu, C. Li, Medium pressure UV-activated peroxymonosulfate for ciprofloxacin degradation: Kinetics, mechanism, and genotoxicity, Chem. Eng. J. 345 (2018) 87–97, https://doi.org/10.1016/j.cej.2018.03.133.

[19] M. Noorisepehr, K. Ghadirinejad, B. Kakavandi, A. Ramazanpour Esfahani, A. Asadi, Photo-assisted catalytic degradation of acetaminophen using peroxymonosulfate decomposed by magnetic carbon heterojunction catalyst, Chemosphere 232 (2019) 140–151, https://doi.org/10.1016/j.chemosphere.2019.05.070.

[20] H.P. A. Annamalai, A. Subramanian, U. Kang, J.S.J. Sun Hee Choi, Activation of Hematite Photoanodes for Solar Water Splitting: Effect of FTO Deformation, J. Phys. Chem. C 2015, 119, 3810−3817. 3 (2015). 10.1021/jp512189c.

[21] Y. Xu, H. Zhang, D. Gong, Y. Chen, S. Xu, Solar water splitting with nanostructured hematite : the role of oxygen vacancy, J. Mater. Sci. 57 (2022) 19716–19729, https://doi.org/10.1007/s10853-022-07885-3.

[22] R. Khaghani, B. Kakavandi, K. Ghadirinejad, E. Dehghani Fard, A. Asadi, Preparation, characterization and catalytic potential of γ-Fe$_2$O$_3$/AC mesoporous heterojunction for activation of peroxymonosulfate into degradation of cyfluthrin insecticide, Microporous Mesoporous Mater. 284 (2019) 111–121, https://doi.org/10.1016/j.micromeso.2019.04.013.

[23] F. Ghanbari, M. Moradi, Application of peroxymonosulfate and its activation methods for degradation of environmental organic pollutants: Review, Chem. Eng. J. 310 (2017) 41–62, https://doi.org/10.1016/j.cej.2016.10.064.

[24] H. Song, L. Yan, J. Jiang, J. Ma, Z. Zhang, J. Zhang, P. Liu, T. Yang, Electrochemical activation of persulfates at BDD anode: Radical or nonradical oxidation? Water Res. 128 (2018) 393–401, https://doi.org/10.1016/j.watres.2017.10.018.

[25] K. Wang, G. Liang, M. Waqas, B. Yang, K. Xiao, C. Zhu, J. Zhang, Peroxymonosulfate enhanced photoelectrocatalytic degradation of ofloxacin using an easily coated cathode, Sep. Purif. Technol. 236 (2020), 116301, https://doi.org/10.1016/j.seppur.2019.116301.

[26] Q. Zhang, D. He, X. Li, W. Feng, C. Lyu, Y. Zhang, Mechanism and performance of singlet oxygen dominated peroxymonosulfate activation on CoOOH nanoparticles for 2,4-dichlorophenol degradation in water, J. Hazard. Mater. 384 (2020), 121350, https://doi.org/10.1016/j.jhazmat.2019.121350.

[27] J. Hu, X. Zeng, G. Wang, B. Qian, Y. Liu, X. Hu, B. He, L. Zhang, X. Zhang, Modulating mesoporous Co$_3$O$_4$ hollow nanospheres with oxygen vacancies for highly efficient peroxymonosulfate activation, Chem. Eng. J. 400 (2020) 125869, https://doi.org/10.1016/j.cej.2020.125869.

[28] S. Xiao, M. Cheng, H. Zhong, Z. Liu, Y. Liu, X. Yang, Q. Liang, Iron-mediated activation of persulfate and peroxymonosulfate in both homogeneous and heterogeneous ways: A review, Chem. Eng. J. 384 (2020) 123265, https://doi.org/10.1016/j.cej.2019.123265.

[29] Q. Qin, T. Liu, J. Zhang, R. Wei, S. You, Y. Xu, Facile synthesis of oxygen vacancies enriched α-Fe$_2$O$_3$ for peroxymonosulfate activation: A non-radical process for sulfamethoxazole degradation, J. Hazard. Mater. 419 (2021) 126447, https://doi.org/10.1016/j.jhazmat.2021.126447.

[30] M. Ding, W. Chen, H. Xu, Z. Shen, T. Lin, K. Hu, C. hui Lu, Z. Xie,, Novel α-Fe$_2$O$_3$/MXene nanocomposite as heterogeneous activator of peroxymonosulfate for the degradation of salicylic acid, J. Hazard. Mater. 382 (2020), 121064, https://doi.org/10.1016/j.jhazmat.2019.121064.

[31] F. Ji, C. Li, X. Wei, J. Yu, Efficient performance of porous Fe$_2$O$_3$ in heterogeneous activation of peroxymonosulfate for decolorization of Rhodamine B, Chem. Eng. J. 231 (2013) 434–440, https://doi.org/10.1016/j.cej.2013.07.053.

[32] R. Abe, Recent progress on photocatalytic and photoelectrochemical water splitting under visible light irradiation, J Photochem Photobiol C: Photochem Rev 11 (2010) 179–209, https://doi.org/10.1016/j.jphotochemrev.2011.02.003.

[33] L.R. Nagappagari, H. Lee, B. Jeong, K. Lee, Energy and environmental applications of Sn4+/Ti4+ doped α-Fe2O3@Cu2O/CuO photoanode under optimized photoelectrochemical conditions, Environ. Pollut. 271 (2021), 116318, https://doi.org/10.1016/j.envpol.2020.116318.

[34] P. Liao, E.A. Carter, Hole transport in pure and doped hematite, J. Appl. Phys. 112 (2012) 1775–1781, https://doi.org/10.1063/1.4730634.

[35] Y. Ling, G. Wang, D.A. Wheeler, J.Z. Zhang, Y. Li, Sn-doped hematite nanostructures for photoelectrochemical water splitting, Nano Lett. 11 (2011) 2119–2125, https://doi.org/10.1021/nl200708y.

[36] K. Sivula, R. Zboril, F. Le Formal, R. Robert, A. Weidenkaff, J. Tucek, J. Frydrych, M. Grätzel, Photoelectrochemical water splitting with mesoporous hematite prepared by a solution-based colloidal approach, J. Am. Chem. Soc. 132 (2010) 7436–7444, https://doi.org/10.1021/ja101564f.

[37] L. Wu, Y. Yu, Q. Zhang, J. Hong, J. Wang, Y. She, A novel magnetic heterogeneous catalyst oxygen-defective CoFe$_2$O$_{4-x}$ for activating peroxymonosulfate, Appl. Surf. Sci. 480 (2019) 717–726, https://doi.org/10.1016/j.apsusc.2019.03.034.

[38] J. Yu, T. Zeng, H. Wang, H. Zhang, Y. Sun, L. Chen, S. Song, L. Li, H. Shi, Oxygen-defective MnO$_{2-x}$ rattle-type microspheres mediated singlet oxygen oxidation of organics by peroxymonosulfate activation, Chem. Eng. J. 394 (2020) 124458, https://doi.org/10.1016/j.cej.2020.124458.

[39] S. Guo, H. Wang, W. Yang, H. Fida, L. You, K. Zhou, Scalable synthesis of Ca-doped α-Fe$_2$O$_3$ with abundant oxygen vacancies for enhanced degradation of organic pollutants through peroxymonosulfate activation, Appl. Catal. B Environ. 262 (2020), 118250, https://doi.org/10.1016/j.apcatb.2019.118250.

[40] M. Wang, S. Li, J. Kang, Y. Tang, J. Wang, Z. Xu, J. Liu, Enhanced tetracycline degradation by N-C codoped Fe2O3 with rich oxygen vacancies in peroxymonosulfate assisting photoelectrochemical oxidation system : performance, mechanism and degradation pathway, Chem. Eng. J. 451 (2023), 138611, https://doi.org/10.1016/j.cej.2022.138611.

[41] M. Machreki, T. Chouki, M. Martelanc, L. Butinar, B.M. Vodopivec, S. Emin, Preparation of porous α-Fe$_2$O$_3$ thin films for efficient photoelectrocatalytic degradation of basic blue 41 dye, J. Environ. Chem. Eng. 9 (2021), https://doi.org/10.1016/j.jece.2021.105495.

[42] P.S. Shinde, A. Annamalai, J.H. Kim, S.H. Choi, J.S. Lee, J.S. Jang, Photoelectrochemical, impedance and optical data for self Sn-diffusion doped Fe$_2$O$_3$ photoanodes fabricated at high temperature by one and two-step annealing methods, Data Br. 5 (2015) 796–804, https://doi.org/10.1016/j.dib.2015.10.031.

[43] Y. Ling, G. Wang, D.A. Wheeler, J.Z. Zhang, Y. Li, Sn-doped hematite nanostructures for photoelectrochemical water splitting, Nano Lett. 11 (5) (2011) 2119–2125.

[44] H. Zhang, J. Song, C. Liu, Immobilization of α- Fe2O3 Nanoparticles on PET Fiber by Low Temperature Hydrothermal Method, Ind. Eng. Chem. Res. 52 (2013) 7403–7412, https://doi.org/10.1021/ie400019t.

[45] S. Emin, M. De Respinis, T. Mavrič, B. Dam, M. Valant, W.A. Smith, Photoelectrochemical water splitting with porous α-Fe$_2$O$_3$ thin films prepared from Fe/Fe-oxide nanoparticles, Appl. Catal. A 523 (2016) 130–138, https://doi.org/10.1016/j.apcata.2016.06.007.

[46] T. Yamashita, P. Hayes, Analysis of XPS spectra of Fe2 + and Fe3+ ions in oxide materials, Appl. Surf. Sci. (2008) 2441–2449, https://doi.org/10.1016/j.apsusc.2007.09.063.

[47] Y. Ling, G. Wang, J. Reddy, C. Wang, J.Z. Zhang, Y. Li, Angewandte The Influence of Oxygen Content on the Thermal Activation of Hematite Nanowire, Angew. Chem. Int. Ed. (2012) 4074–4079, https://doi.org/10.1002/anie.201107467.

[48] C.M. Tian, W. Li, Y.M. Lin, Z.Z. Yang, L. Wang, Y.G. Du, H.Y. Xiao, L. Qiao, J. Y. Zhang, L. Chen, D. Qi, K.H.L. Zhang, Electronic Structure, Optical Properties, and Photoelectrochemical Activity of Sn-Doped Fe$_2$O$_3$ Thin Films, J. Phys. Chem. C (2020) 12548–12558, https://doi.org/10.1021/acs.jpcc.0c02875.

[49] H. Lim, H. Yang, J.W. Kim, J. Bae, J. Kim, B. Jeong, E. Crumlin, S. Park, B.S. Mun, In situ analysis of post-annealing effect on Sn-doped indium oxide films, J. Appl. Phys. (2016) 205306, https://doi.org/10.1063/1.4968010.

[50] B.Z. Zhou, S. Wu, L. Qin, L. Li, L. Li, Xi. Li,, Modulating oxygen vacancies in Sn-doped hematite film grown on silicon microwires for photoelectrochemical water oxidation, J. Mater. Chem. A (2018) 15593–15602, https://doi.org/10.1039/C8TA03643H.

[51] Q. Yang, J. Du, J. Li, Y. Wu, Y. Zhou, Y. Yang, D. Yang, H. He, Thermodynamic and Kinetic In fl uence of Oxygen Vacancies on the Solar Water Oxidation Reaction of α-Fe2O3 Photoanodes, ACS Appl. Mater. Interfaces 12 (10) (2020) 11625–11634, https://doi.org/10.1021/acsami.9b21622.

[52] C. Xiao, Z. Zhou, L. Li, S. Wu, X. Li, Tin and Oxygen-Vacancy Co-doping into Hematite Photoanode for Improved Photoelectrochemical Performances, Nanoscale Res. Lett. 15 (2020) 54, https://doi.org/10.1186/s11671-020-3287-1.

[53] J. Kim, H. Kim, M. Lee, D. Lee, J. Lee, Y.H. Jang, J. Bae, J. Lee, Atomistic aspects of carrier concentration variation in post-annealed indium tin oxide films, J. Phys. D Appl. Phys. (2015), 395307, https://doi.org/10.1088/0022-3727/48/39/395307.

[54] L. Gong, J. Xie, X. Liang, J. Xiong, S. Yi, X. Zhang, C.M. Li, Tailoring surface states by sequential doping of Ti and Mg for kinetically enhanced hematite photoanode, J. Colloid Interface Sci. 542 (2019) 441–450.

[55] A. Duret, M. Grätzel, Visible light-induced water oxidation on mesoscopic α-Fe2O3 films made by ultrasonic spray pyrolysis, J. Phys. Chem. B 109 (36) (2005) 17184–17191.

[56] J. Cai, S. Li, Z. Li, J. Wang, Y. Ren, G. Qin, Electrodeposition of Sn-doped hollow α-Fe2O3 nanostructures for photoelectrochemical water splitting, J. Alloy. Compd. 574 (2013) 421–426, https://doi.org/10.1016/j.jallcom.2013.05.152.

[57] E.S. Cho, M.J. Kang, Y.S. Kang, Enhanced photocurrent density of hematite thin films on FTO substrates : effect of post-annealing, PCCP (2015) 16145–16150, https://doi.org/10.1039/C5CP01823D.

[58] A. Rauf, M. Adil, S.A. Mian, G. Rahman, E. Ahmed, Z. Mohy, U. Din, W. Qun, Tuning the optoelectronic properties of hematite with rhodium doping for photoelectrochemical water splitting using density functional theory approach, Sci. Rep. (2021) 1–11, https://doi.org/10.1038/s41598-020-78824-y.

[59] X. Chen, Y. Fu, L. Hong, T. Kong, X. Shi, G. Wang, L. Qu, S. Shen, Interface and surface engineering of hematite photoanode for efficient solar water oxidation Interface and surface engineering of hematite photoanode for efficient solar water oxidation, J. Chem. Phys. (2020), 244707, https://doi.org/10.1063/5.0009072.

[60] H.P.A. Annamalai, A. Subramanian, U. Kang, Activation of Hematite Photoanodes for Solar Water Splitting: Effect of FTO Deformation, J. Phys. Chem. C 119 (3810–3817) (2015) 3, https://doi.org/10.1021/jp512189c.

[61] A. Annamalai, H.H. Lee, S.H. Choi, S.Y. Lee, E. Gracia-Espino, A. Subramanian, J. Park, K.J. Kong, J.S. Jang, Sn/Be Sequentially co-doped Hematite Photoanodes for Enhanced Photoelectrochemical Water Oxidation: Effect of Be2+ as co-dopant, Sci. Rep. 6 (2016) 1–11, https://doi.org/10.1038/srep23183.

[62] P. Kumar, P. Sharma, R. Shrivastav, S. Dass, V.R. Satsangi, Electrodeposited zirconium-doped α-Fe2O3 thin film for photoelectrochemical water splitting, Int. J. Hydrogen Energy 36 (2011) 2777–2784, https://doi.org/10.1016/j.ijhydene.2010.11.107.

[63] M. Machreki, T. Chouki, G. Tyuliev, D. Žigon, B. Ohtani, A. Loukanov, P. Stefanov, Defective TiO2 Nanotube Arrays for Efficient Photoelectrochemical Degradation of Organic Pollutants, ACS Omega 8 (24) (2023) 21605–21617, https://doi.org/10.1021/acsomega.3c00820.

[64] J. Ding, Z. Dai, F. Qin, H. Zhao, S. Zhao, R. Chen, Z-scheme BiO1-x Br/Bi2O2CO3 photocatalyst with rich oxygen vacancy as electron mediator for highly efficient degradation of antibiotics, Appl. Catal. B, Environ (2017) 281–291. 10.1016/j.apcatb.2016.12.018.

[65] J.Z.Z. Geng, X. Kong, W. Chen, H. Su, Y. Liu, F. Cai, G. Wang, Oxygen Vacancies in ZnO Nanosheets Enhance CO2 Electrochemical Reduction into CO, Angew. Chem. Int. Ed. 57 (2018) https://doi.org/10.1002/Anie.201907954.

[66] J. Bao, X. Zhang, B. Fan, J. Zhang, M. Zhou, W. Yang, X. Hu, H. Wang, B. Pan, Y., Xie, Ultrathin Spinel-Structured Nanosheets Rich in Oxygen Deficiencies for Enhanced Electrocatalytic Water Oxidation, Angew. Chem. Int. Ed. 54 (1–7) (2015), https://doi.org/10.1002/anie.201502226.

[67] M. Wang, Y. Cui, H. Cao, P. Wei, C. Chen, X. Li, J. Xu, Activating peroxydisulfate with Co3O4/NiCo2O4 double-shelled nanocages to selectively degrade bisphenol A – A nonradical oxidation process, Appl. Catal. B Environ. 282 (2021), 119585, https://doi.org/10.1016/j.apcatb.2020.119585.

[68] Y. Wang, Z. Chi, C. Chen, C. Su, D. Liu, Y. Liu, X. Duan, S. Wang, Facet- and defect-dependent activity of perovskites in catalytic evolution of sulfate radicals, Appl. Catal. B Environ. 272 (2020), 118972, https://doi.org/10.1016/j.apcatb.2020.118972.

[69] M.S. Koo, X. Chen, K. Cho, T. An, W. Choi, X. Chen, K. Cho, T. An, W. Choi, In Situ Photoelectrochemical Chloride Activation Using a WO3 Electrode for Oxidative Treatment with Simultaneous H2 Evolution under Visible Light, Environ. Sci. Tech. 53 (2019) 9926–9936, https://doi.org/10.1021/acs.est.9b02401.

[70] J. Luo, M. Hepel, Photoelectrochemical degradation of naphthol blue black diazo dye on WO3 film electrode, Electrochim. Acta 46 (2001) 2913–2922. https://doi:10.1016/S0013-4686(01)00503-5.

[71] A.U.R. Bacha, I. Nabi, H. Cheng, K. Li, S. Ajmal, T. Wang, L. Zhang, Photoelectrocatalytic degradation of endocrine-disruptor bisphenol – A with significantly activated peroxymonosulfate by Co-BiVO4 photoanode, Chem. Eng. J. 389 (2020), 124482, https://doi.org/10.1016/j.cej.2020.124482.

[72] M. Zhang, Y. Gong, N. Ma, X. Zhao, Promoted photoelectrocatalytic degradation of BPA with peroxymonosulfate on a MnFe2O4 modified carbon paper cathode, Chem. Eng. J. 399 (2020), 125088, https://doi.org/10.1016/j.cej.2020.125088.

[73] J. Li, Y. Wang, S. Zhao, A.K. Jan, X. Zhang, X. Zhao, Electrospun nanostructured Co3O4/BiVO4 composite films for photoelectrochemical applications, J. Colloid Interface Sci. 539 (2019) 442–447, https://doi.org/10.1016/j.jcis.2018.12.081.

[74] Q. Xiang, J. Yu, P.K. Wong, Quantitative characterization of hydroxyl radicals produced by various photocatalysts, J. Colloid Interface Sci. 357 (2011) 163–167, https://doi.org/10.1016/j.jcis.2011.01.093.

[75] G.L. Newton, J.R. Milligan, Fluorescence detection of hydroxyl radicals, Radiat. Phys. Chem. 75 (2006) 473–478, https://doi.org/10.1016/j.radphyschem.2005.10.011.

[76] E. Brillas, I. Sirés, C. Arias, P.L. Cabot, F. Centellas, R.M. Rodríguez, J.A. Garrido, Mineralization of paracetamol in aqueous medium by anodic oxidation with a boron-doped diamond electrode, Chemosphere 58 (2005) 399–406, https://doi.org/10.1016/j.chemosphere.2004.09.028.

[77] J.B. Quintana, S. Weiss, T. Reemtsma, Pathways and metabolites of microbial degradation of selected acidic pharmaceutical and their occurrence in municipal wastewater treated by a membrane bioreactor, Water Res. 39 (2005) 2654–2664, https://doi.org/10.1016/j.watres.2005.04.068.

[78] Zucconi, F.; Monaco, A.; Forte, M., Phytotoxins during the stabilization of organic matter. in: gasser JKR composting of agricultural and other wastes, *Elsevier Applied Science.* (1985) 73–86.

[79] P. Mañas, J., De las Heras, Phytotoxicity test applied to sewage sludge using Lactuca sativa L. and Lepidium sativum L. seeds, Int. J. Environ. Sci. Technol. 15 (2018) 273–280, https://doi.org/10.1007/s13762-017-1386-z.